Title

THz Imaging System for *in vivo* Human Cornea

Authors

Sung, Shijun
Selvin, Skyler
Bajwa, Neha
et al.

THz imaging system for *in vivo* human cornea

Shijun Sung,
UCLA Dept. of Electrical Engineering, Los Angeles, CA 90095

Skyler Selvin,
UCLA Dept. of Electrical Engineering, Los Angeles, CA 90095

Neha Bajwa,
UCLA Dept. of Bioengineering, Los Angeles, CA 90095 USA

Somporn Chantra,
UCLA Dept. of Ophthalmology, Los Angeles, CA 90095 USA

Bryan Nowroozi,
UCLA Dept. of Bioengineering, Los Angeles, CA 90095

James Garritano,
UCLA Dept. of Bioengineering, Los Angeles, CA 90095 USA

Jacob Goell,
UCLA Dept. of Bioengineering, Los Angeles, CA 90095 USA

Alex Li,
UCLA Dept. of Bioengineering, Los Angeles, CA 90095 USA

Sophie X. Deng,
UCLA Dept. of Ophthalmology, Los Angeles, CA 90095 USA

Elliott Brown,
Wright State University Dept. of Electrical Engineering, Dayton, OH 45435 USA

Warren S. Grundfest, and
UCLA Dept. of Electrical Engineering, Los Angeles, CA 90095; UCLA Dept. of Bioengineering, Los Angeles, CA 90095 USA

Zachary D. Taylor
UCLA Dept. of Electrical Engineering, Los Angeles, CA 90095; UCLA Dept. of Bioengineering, Los Angeles, CA 90095 USA, phone: 858-663-1823; fax: 310-206-2105

Abstract

Terahertz (THz) imaging of corneal tissue water content (CTWC) is a proposed method for early, accurate detection and study of corneal diseases. Despite promising results from *ex vivo* and *in*

S. Dabironezare and N. Llombart are with the Center for Wireless Systems and Technology, TU Delft, Netherlands

Bryan Nowroozi: He is now with Mimeo Labs Inc, Santa Monica, CA 90404 USA.

vivo cornea studies, interpretation of the reflectivity data is confounded by the contact between corneal tissue and rigid dielectric window used to flatten the imaging field. This work develops a novel imaging system and image reconstruction methods specifically for nearly spherical targets such as human cornea. A prototype system was constructed using a 650 GHz multiplier source and Schottky diode detector. Resolution and imaging field strength measurement from characterization targets correlate well with those predicted by the quasioptical theory and physical optics analysis. Imaging experiments with corneal phantoms and *ex vivo* corneas demonstrate the hydration sensitivity of the imaging system and reliable measurement of CTWC. We present successful acquisition of non-contact THz images of *in vivo* human cornea, and discuss strategies for optimizing the imaging system design for clinical use.

Index Terms

Biological and medical imaging; THz imaging of cornea; medical diagnostics; clinical instruments

I. Introduction

THz corneal hydration imaging is unique among other biomedical imaging applications. First, the field of view and target are well defined and display a high degree of uniformity. The geometry of the corneal surface is nearly spherical with a deviation in optical sag less than 1λ at 650 GHz [1–4]. Second, the target tissue thickness range can be measured *a priori* with a high degree of confidence and can be leveraged for deconvolving confounders in THz measurement. Hence, imaging system design and data analysis can focus on a limited number of parameters and unknowns, therefore enabling precise measurement of corneal hydration in vivo.

In related work [1] a non-contact, spherical scanning method for corneal imaging was introduced. The imaging method placed the corneal center of curvature (CoC) coincident with the focal point of an over-dimensioned (optics diameter ≫ individual collimated beam width) 90° off-axis parabolic (OAP) mirror, and scanned a collimated beam parallel to the axis of the mirror over the clear-aperture (CA) of the reflector (Figure 1). There is a one-to-one mapping between CA plane location and corneal surface angular location and complete sampling of the CA results in a solid angle spanning the majority of the cornea [1]. Quasioptical analysis methods were developed to investigate expected spatial resolution and beam coupling efficiency. Physical optics analysis explored the validity of assumptions used in the quasioptical methods. Good agreement was demonstrated between analysis methods for both spatial resolution and coupling [1].

This work details the design, implementation, and characterization of a non-contact, THz corneal imaging system based on [1]. Image reconstruction methods and sampling schemes are discussed. The mapping operation from the scanning coordinates to the spherical target surface is formulated for a circular aperture 90° OAP mirrors. Optimal beam sampling locations were found based on input beam diameters and desired sampling density on target. A prototype imaging system was constructed and used to acquire reflectivity maps of characterization targets. Experimentally obtained spatial resolution and beam coupling

coefficient data was compared to quasioptical theory and physical optics computations [1] and goodness of fit was assessed. Further testing was performed with imaging experiments of drying contact lenses and *ex vivo* porcine eyes. Finally, the first successful non-contact THz imaging of human cornea *in vivo* is presented. The design and implementation details presented in this work will enable the first, clinically feasible, *in vivo* exploration of CTWC using THz technology.

II. Imaging system optical layout

The system optical layout in Figure 2 depicts the input and output beams multiplexed demultiplexed by a beam splitter that optically collocates the THz emitter and detector [1]. The imaging system design was organized into three independent subsystems that each transmit and receive collimated beams: (1) Transceiver subsystem, (2) Scanning subsystem, and (3) Imaging mirror.

The plane mirrors labeled "x-scan" and "y-scan" allow transverse positioning of the collimated beam anywhere within the OAP mirror's CA. The imaging mirror is radially symmetric about its focal point thus, if the cornea CoC is coincident with the OAP mirror's focal point, all incoming beam paths are orthogonal to the spherical surface. Further, all reflected beams, independent of scan mirror position, will arrive at the detector feedhorn with identical beam convergence angle and beam transverse location and extent.

The concept is demonstrated with the three superimposed beam paths in Figure 2. Parallel bundles of rays were traced for three separate x-scan mirror locations and a stationary y-scan location. The ray paths show that all 3 illumination beams result in identical received beams at the detector thus enabling mapping of normal incidence reflectivity of the cornea while keeping the source, detector, and target stationary.

III. Coordinate Transformations and Mapping for Image Reconstruction

The forward mapping from the (x,y) scanning coordinates of the x- and y-scan mirrors to the spherical coordinates of the cornea (θ, ϕ), are given in equations (1) and (2), which describe the transformation of the beam centroid location. The reverse mapping from (θ, ϕ) to (x,y) coordinates are given in equations (3) and (4). The relations are illustrated in Figure 1 and are specific for a 90° OAP mirror.

$$\theta = \frac{\pi}{2} - \tan^{-1}\left(\frac{\sqrt{x^2+y^2}}{4f_0} - \frac{f_0}{\sqrt{x^2+y^2}} \right) \quad (1)$$

$$\phi = \tan^{-1}\left(\frac{y}{x} \right) \quad (2)$$

$$x = 2f_0 \cos(\phi) \left[\tan\left(\frac{\pi}{2} - \theta\right) + \sec\left(\frac{\pi}{2} - \theta\right) \right] \quad (3)$$

$$y = x \tan(\phi) \quad (4)$$

These relations perform a conformal and orthogonal mapping from the rectilinear sampling coordinate to the angular coordinate of target surface. f_0 denotes parent focal length of the parabolic mirror, whose focal point is at $(x, y, z) = (0, 0, 0)$, and the parabolic vertex is at $(x, y, z) = (0, 0, -f_0)$. The mirror's clear aperture in Figure 1(b) is at $z = 0$ whose center is at $(x, y) = (2f_0, 0)$. The apex (center) of the cornea is pierced by the x-axis and is located at $(x, y, z) = (8 \text{ mm}, 0, 0)$, which maps to $(R, \theta, \phi) = (8 \text{ mm}, +\pi/2, 0)$ in spherical coordinates. Inspection of Figure 1, and equations (1)–(4) confirms no dependence on the height, z, above the mirror and no dependence on the corneal radius of curvature, R_c. All rays reaching the cornea are orthogonal to the spherical surface, and each pixel position on target is fully described by the azimuthal (ϕ) and elevation (θ) angles which correspond to unique (x, y) coordinates.

Three different beam scanning paths ("sampling grids") were considered for imaging of a spherical surface. These are displayed in Figure 3(a)–(f) for a 76.2 mm CA, 25.4 mm PFL, 90° OAP mirror. The grids and associated mappings adhere to the standard spherical coordinate, thus the vertical axis in the plots of the OAP clear aperture corresponds to the x-axis and the horizontal axis corresponds to the y-axis.

The sampling grid and mapping displayed in Figure 3(a),(b) is termed "Equiangular scanning" which samples the sphere in equal increments (e.g $10° \rightarrow \pi/18$) in both the θ and ϕ directions, represented by the longitudinal (blue) latitude (red) traces, respectively. The black circular markers (●) represent the intersections of the θ-scan ϕ-scan lines, and thus sampling locations in the x-y plane. The fixed-ϕ-varying-θ paths (longitude) are mapped to straight lines, distributed radially, in the aperture space at $(x, y) = (0, 0)$. The fixed-θ, varying-ϕ paths (latitude) are mapped to circles concentric at the focus $(x = 0, y = 0)$. Their radii were calculated with Equation (3) and $\phi = 0$.

The mapping of the equiangular scanning confirms that the beam scanning must be the densest towards the near edge of the OAP CA and then progressively less dense as the beam is moved radially outward from the corneal center of curvature. This observation is consistent with the optical power of the OAP, which is inversely proportional to the distance, R_s, from the parent focal point to any constant θ line.

The sampling grid in Figure 3(c) and (d) is termed "orthodromic" and is a modification of the equiangular scanning. In this sampling distribution the circular paths described by scanning ϕ at a given θ (red latitude lines in Figure 3(a),(b)) are replaced by orthodromes which are defined as curves on the surface of a sphere that are formed by the intersection of the sphere and a plane that is coincident with the sphere center point [5]. The planes were

defined by the following three points, where point P3 defines the angle (β) the plane makes with the z-axis.

- P1: $(R_C, \theta, \phi) = (8, \pi/2, -\pi/2)$

- P2: $(R_C, \theta, \phi) = (8, \pi/2, +\pi/2)$

- P3: $(R_C, \theta, \phi) = (8, \beta, 0)$

The spherical coordinates defining the orthodrome scanning path is given in equation (5) and derived from [5].

$$\theta = \cot^{-1}\left(\tan\left(\frac{\pi}{2} - \beta\right)\cos(\phi)\right), \forall \phi \in [-\pi, \pi] \tag{5}$$

The longitude lines in Figure 3(c), (d) are the same as Figure 3(a), (b). Conversely, the "latitude" lines demonstrate comparative decreased curvature closer to the mirror focal point and increased curvature at the extreme periphery of the aperture.

Orthodrome mapping is useful for spot size characterization using spherical edge response, or "knife-edge" targets (e.g. a sphere composed of 1 metallic hemisphere and 1 dielectric hemisphere). Orthodrome mapping produces pixels that are arc-length wise equidistant from the neighboring pixels and all intersections of the latitude and longitudinal lines are orthogonal.

The sampling grid in Figure 3(e), (f) is termed "Uniform-rectilinear" and demonstrates the uniform rectilinear sampling positions in Figure 3(e) mapped onto the corneal spherical surface in Figure 3(f). This sampling grid results in sparse sampling towards the bottom section of the cornea, Therefore the sampling grid need to sufficiently over-sample in the clear-aperture to provide sufficient sampling of the corneal surface. Uniform rectilinear sampling was the most straightforward to implement with linear translation stages, and thus we are motivated to find the sufficient sampling density that permits re-mapping of the raw data into Orthodrome or equiangular sampling coordinates.

IV. Uniform Rectilinear Sampling of an Equiangular Sampling Grid

The system in section V utilized uniform rectilinear sampling, thus we find a sampling density sufficient to resolve critical equiangular and orthodrome sampling given a set of spatial resolution criteria. Inspection of Figure 3 indicates that the equiangular scan paths produce more non-uniform sampling density than the orthodrome paths. Therefore, if the rectilinear sampling density can resolve an equiangular grid, it will also be sufficient to resolve an orthodrome grid of the same resolution.

The desired sampling density was set by the arc length between sampling points on target (cornea) equal to the optimal spatial resolution determined in [1]. The corresponding angular separation is found at the equator $d \rightarrow \phi(\theta=\pi/2)$ (Figure 4(a)). Then, an "equiangular" arrangement of collimated beams was identified that yielded the largest number of "unclipped" beams in the mirror aperture.

Geometry relevant to the optimizing beam packing is shown in Figure 4 where ω_0 is the input beam radius, δ (Figure 4(b)) is a multiplicative factor which determines the offset between the beam centroid and mirror edge so that the effect of diffraction is minimized. A is the mirror CA dimeter, R_{s0} is the first scan radius, and γ is the angular resolution defined by the number of beams (N) and the pre-determined linear spatial resolution d. Examples of increasing R_{s0} for increasing N are shown in Figure 4 (c),(d).

Figure 3(a), (b) demonstrates that the maximum sampling density in the equiangular scheme occurs on the first scan radius and the position of the subsequent scan radii are defined by the position of the first. Thus, the optimization was performed over the competing factors of (1) increasing the first scan radius to accommodate more beams and (2) the subsequent decrease in total scan radii and potential decrease in the number of unclipped beams.

The optimal packing of beams in the equiangular coordinate and corresponding sufficient, uniform rectilinear sampling density were determined for the following two sets of parameters: (1) A = 76.2 mm, f_0 = 25.4 mm, ω_0 = 7.6 mm, ω_1 = 1.5 mm, and (2) A = 76.2 mm, f_0 = 25.4 mm, ω_0 = 10 mm, ω_1 = 1.5 mm. It was determined in [1] that parameter set 1 minimized the average focused radius on the cornea while ω_0 = 10 mm in parameter set 2 was the closest to ω_0 = 7.6 mm achievable experimentally with a 26 dB gain feedhorn coupled source and commercially available OAP mirrors. In both cases the minimum predicted spot size was ω_1 1.5 mm therefore the angular resolution was computed with d = 1.5 mm.

The equiangular sample locations indicated by the intersection of the equiangular longitude and latitude contours lines are denoted by the ($\bigcirc$) marker in Figure 5(a),(d). Intersections that do not have markers correspond to locations whose minimum distance between centroid and aperture was less than one collimated beam radius (ω_0). Figure 5(b),(e) superimposes beam 1/e contour lines centered at the sampling locations from Figure 5(a),(d) and demonstrate substantial decrease in beam overlap for increasing R_s.

The lines in Figure 5(a),(d) subtend regions (shaded) that fall within the beam area covered by the beam contours in Figure 5(b),(e). Uniform rectilinear sampling grids were superimposed on the shaded regions and the uniform grid density was modulated until the largest integer center-to-center separation in millimeters was identified that places at least one sample in every shaded location. A minimum of 5 mm center-to-center separation was identified sufficient for both the optimal input beam radius (Figure 5(a)-(c)) and the realized input beam radius (Figure 5(d)-(f)).

V. THz corneal hydration imager Implementation

A prototype system, with the optical layout in Figure 2 and block diagram in Figure 6(a), was constructed with a solid-state frequency-modulated continuous wave THz source (Virginia Diodes) centered at 650 GHz. The detector was a WR1.5 waveguide mounted Schottky diode detector (ZBD) (Virginia Diodes, VA) with a 500GHz-700GHz detection bandwidth. Both the source and detector were coupled to diagonal feedhorn antennas with 26 dB of directional gain.

To mitigate the effects of standing waves, the output was frequency modulated over ~2 GHz at a rate of 100 kHz, providing a frequency bandwidth that exceeds the expected full etalon period of the optical path. The source was also amplitude modulated at ~900 Hz, and the rectified signal from the ZBD was detected with a Lock-in amplifier (Stanford Research Systems, CA) using an integration time of 3 milliseconds (ms). The system used 25.4 mm PFL, 50.8 mm CA, 90° OAP mirrors to collimate radiation from the multiplier chain and focus reflected radiation into the detector aperture. The combination of feedhorn directivity and OAP PFL yielded a ~ 10 mm collimated 1/e field radius as measured with a knife-edge target. The imaging mirror was a 76.2 mm CA, 25.4 mm PFL OAP. Beam scanning was performed with two 50.8 mm diameter gold-coated plane mirrors. A CAD design of the system and an image of the constructed system are displayed in Figure 6(b) and (c) respectively.

The angular coverage produced by the imaging mirror is detailed in Figure 7 where the gray contour is the extent of the cornea and the black contour is the mapped CA of the scanning OAP and hence the angular extent of all possible beam centroids. These contour lines are superimposed on a set of mapped orthodrome scan lines that subtend the mirror CA. The FOV is not concentric with the corneal perimeter and the significant area below the cornea was accessed.

A. Imaging Results

Three spherical targets with $5/16'' = 7.93$ mm radii of curvature were imaged. (1) A brass sphere to evaluate the uniformity of the FOV and its relation to the modeled coupling efficiency. (2) A polypropylene sphere with a 3 mm wide strip of Al Tape positioned such that the center of the strip was collinear with an orthodrome of the sphere. This target was rotated 90 degrees between image acquisitions to confirm that the mapping and sampling distributions behaved as expected. (3) A "checkerboard" target constructed with hypohemispherical sections of polypropylene and brass. This target provided two orthogonal knife edges on one surface thus removing the need to realign/reposition for characterization along different axes. CAD drawings of the strip and checkerboard target are shown in Figure 8(a). The images were sampled using the uniform rectilinear grid pattern (Figure 3(e),(f)) with a 5 mm step size. The translation of pixel data from aperture plane to sphere was performed by first up sampling the aperture space image and then performing the mapping described by equations (1) – (4).

The characterization target imaging results are displayed in Figure 8(b). The photographs in the top row demonstrate the mounting orientation in the system. The middle row contains the 2D image of the mirror aperture plane (from here on referred to as the raw image), and the bottom row contains the raw data mapped to a 7.93 mm radius sphere using equations (3), (4) (from here on referred to as the mapped image).

The image of the brass sphere displays an increase in signal from the top of the FOV to the bottom with a spatial gradient that is generally radially symmetric about the mirror focal point. Assuming uniform reflectivity across the brass, this signal intensity is consistent with contrast predicted by coupling coefficient variation described in equation (6) [1]. There are

some breaks in the radial symmetry of the reflected signal on the outer periphery of the mirror, which may be due to diffraction or suboptimal alignment.

The vertically oriented aluminum strip displays similar signal profile. Signal intensity increases from the top of the FOV to the bottom with some artifacts. It is noted that the apparent strip width widens from top to bottom, which is consistent with the expected increase in spot size (for a 10 mm input radius) as the radial distance from the target vertical axis and collimated beam centroid location is decreased [1].

The mapped THz image of the horizontal strip maintains a fairly constant apparent thickness although there are local extrema in the observed signal. Close inspection of the visible images reveals a slightly rough surface profile along both the center and the edges of the tape and we believe this is primarily responsible for the observed signal variation.

The checkerboard target serves as a clear demonstration of the asymmetry of the FOV about the OAP mirror optical axis. The intersection of the adjacent brass and polypropylene quarter spheres were aligned with the optical axis and this intersection is above the center of the FOV for the mapped image (bottom right of Figure 8). The edges also appear to be somewhat less sharp that that acquired with the Al tape strip target suggesting that the variation in edge height between dielectric and metallic regions strongly contribute to the overall contrast.

VI. Data Fits to Quasioptical and Physical Optics Results

The desired equiangular or orthodromic sampling locations were defined and then mapped to scan trajectories in aperture plane. These scan trajectories were then superimposed on the raw image data and profiles along these trajectories were analyzed. All THz images in the aperture plane space were masked by a circle with radius $A/2-\omega_0$ to mitigate aberrations due to beam clipping. The brass sphere image is used to understand the signal intensity profile variation, and the Al strip and "checkerboard" images are used to determine the effective spatial resolution of the imaging system.

A. Brass Sphere Analysis: Coupling Coefficient Fits

The brass sphere was assumed to have negligible variation in THz reflectivity across the imaged area. The raw data was interpolated and sampled at equiangular scan lines (Figure 3(a),(b)) where the longitude and latitude contours were spaced at ~ 5 degrees. The brass sphere data was expected to demonstrate radial symmetry about the mirror focal point. The observed imaging field intensity profile arises from the coupling efficiency of the input and output beam: *i.e.* the spatial similarity of the magnitude and phase of the input and output beams. The coupling efficiency $K(q_0, q_3)$ is computed with equation (6) [6] at the beam splitter location in Figure 2 for an input beam radius of 10 mm, where $\omega_{0,3}$ and $R_{0,3}$ are the input and output waists and radii of curvature respectively [1].

$$K(q_0, q_3) = \frac{4}{\left(\frac{\omega_0}{\omega_3} + \frac{\omega_3}{\omega_0}\right)^2 + \left(\frac{\pi\omega_0\omega_3}{\lambda}\right)^2 \left(\frac{1}{R_3} - \frac{1}{R_0}\right)^2} \quad (6)$$

The scan paths in Figure 9(a),(b) corresponding to the image profiles in Figure 9(c),(d) are color coded and the arrows in Figure 9(a),(b) denote the direction of increasing arc length which corresponds to the horizontal axis of Figure 9 (c),(d). Image profiles corresponding to the longitude scan lines in Figure 9 (a) are displayed in Figure 9 (c) and include a superimposed fit to equation (6). The image profiles were normalized to data obtained from a flat Al target placed such that the surface was coincident with the center of curvature of the brass sphere, and 0 reflection obtained by removing all targets from the imaging system.

The coupling coefficient is dependent on four variable parameters: (1) input radius of curvature, (2) output radius of curvature, (3) input spot size, and (4) output spot size. The agreement between theory and data for normalized return signal strongly supports the accuracy of quasioptical theory as applied to corneal imaging [1]. The deviation from theory at the extrema of each profile suggests that diffraction contributes significantly to the measured signal at $1 \cdot \omega_0$ from the mirror aperture edge.

B. Vertical and horizontal metallic strip images: Spatial resolution fits

The metallic strip images were analyzed with the orthodromic scan lines. These lines ensure that the scan path is always orthogonal to the reflectivity discontinuities (edges) of the target features.

$$\Delta(d) = 2(d_0 - d) \quad (7)$$

$$C_b(d) = A \left[1 - \Phi\left(\frac{\Delta(d) - D}{\omega_1}\right) + Q\left(\frac{\Delta(d) + D}{\omega_1}\right) \right] + B \quad (8)$$

Equation (7) defines the arc (chord) length d along the surface of the cornea. Data from the Orthodromic profiles orthogonal to the center line of the bar in the vertical and horizontal positions (Figure 10(a) and Figure 10 (b) respectively) were fit to equation (8) which describes the convolution of a 1D Gaussian distribution of spot size ω_{01} with a rect function of width D and center located at d_0. The functions Φ (·) and 4 Q(·) are the left and right sided integral of standard normal, respectively [7]. Offset parameters A and B were included to improve the fit. The long dimension of the strip was much larger than the transverse extent of the focused beam so it was sufficient to model the data with a 1D convolution.

The profiles and superimposed fits are displayed in Figure 10(c) and Figure 10(d) for the vertical and horizontal orientations respectively. Additionally, the full width at half max (FWHM) as defined by the FWHM of equation (8) informed by the extracted fit parameters are demarcated (○). As evidenced by Figure 10(e),(f) the extracted FWHM is substantially less than 3 mm (the width of the Al bar and thus lower limit of the convolved width) with the vertical bar FWHM ranging from 1.1 mm – 1.95 mm and the horizontal bar ranging from 1.55 mm – 2.25 mm. This observation may be due to the geometric surface discontinuities between the Al tape and polypropylene ball which manifest as visible wrinkles in Figure 8(b). We believe that when the tape surface normal is not parallel to the

normal of the underlying spherical surface, the large optical path lengths result in the beam walking away from the detector feedhorn creating a confocal like behavior. This may explain why the measured tape thickness is smaller than physical thickness.

The FWHM data from the fits to the vertical bar is plotted against mirror radius in Figure 10(e) with the least squares fit line superimposed on the data. While the FWHM are narrower than what was anticipated, the fits display a strong negative correlation between mirror scan radius (R_s) and measured apparent spot size; behavior consistent with that computed for in input field radius (ω_0) of ~ 10 mm. The extracted FWHM for the horizontal bar orientation are displayed in Figure 10(f) as a function of orthodrome angle with respect the central orthodrome with the average of the data superimposed. The data demonstrates some variation but the correlation between spot size and angle is ρ ~0.05 supporting the expected independence of focused spot size over a large angle for a given scan radius.

C. Step response fits

The checker board images were also analyzed with orthodrome scan lines and the extracted image profiles were fit to equation (9) and (10) for rising edge and falling edge response respectively. Equation (9) and (10) describe the convolution of a Gaussian beam (field radius ω_0) with a unit step function centered at d = d_0. The amplitude factor A and offset B were included to maximize goodness of fit and Equations (9) and (10) are related by $C_\Phi(d) = -C_Q(d) + A + 2B$. The center (~ $2\omega_0$ width) area of the FOV was ignored to avoid artifacts due to the presence of the checker board corners.

$$C_\Phi(d) = A \cdot \Phi\left(\frac{\Delta(d)}{\omega_1}\right) + B \quad (9)$$

$$C_Q(d) = A \cdot Q\left(\frac{\Delta(d)}{\omega_1}\right) + B \quad (10)$$

The horizontal orthodrome cuts and associated fits are displayed in Figure 11(a), (c), and (e). Eight cuts were analyzed comprising of the bottom and top regions of the FOV (labeled 1-8 in Figure 11(a)).

The expected focused field radius for a collimated input beam of radius 10 mm, computed with quasioptical theory (−) and physical optics (□) based simulations [1], are superimposed on the extracted spot field radii (Figure 11(e)). The results are consistent with theory and demonstrate a maximum deviation from the focused spot radius curve [1] of 0.473 mm and a standard deviation of 0.233 mm.

Figure 11(c) shows that for most of the profiles 1 through 13, the signal falls off after the peak of the step response. The contours of constant coupling efficiency and focused beam radius and are not co-linear with the orthodrome lines used to ascertain the beam radius. A

deconvolution of spatially varying coupling efficiency and the introduction of a spatially varying focused beam radius may improve the fits.

Seven vertical orthodrome profiles and associated fits are displayed in Figure 11(b), (d), and (f). The extracted focused field radius is plotted vs orthodrome angle and the expected spot size at the mirror radius corresponding to the mapped target edge location is superimposed. There is a good agreement in fit between the measured data and the field radius computed with both quasioptical and physical optics analysis and the results support the relative invariance of the spot size to edges at the spherical target equator. The measured peak deviation was 0.175 mm and the standard deviation was 0.105 mm.

D. Characterization target limitations

The combination of optical path length, low f/# OAPs, and high source/detector directivity resulted in a system that was sensitive to misalignment between the mirror focal point and corneal RoC. This manifests as a sensitivity to surface discontinuities (geometric) which was observed in the characterization target data. The tape strip targets and, to a lesser extent, the checkerboard target both exhibited raised edges and uncontrollable surface roughness which confounded the acquisition of uncluttered resolution data. While these efforts reveal difficulties in characterizing the beam profile on target, there is limited concern for these issues affecting *in vivo* corneal imaging as human cornea surface roughness (~ 15 um) [8, 9] is minimal.

E. Comment on spatial resolution

The observed spatial resolution in the characterization target data exceeds what was predicted from the simulated spot size on target. We hypothesize that this behavior was due to the "confocal" nature of the imaging system, in which the source and detector apertures were on the order of a wavelength in size and are co-focused at the imaging plane.

The radius of curvature (RoC) of incident beam at the target surface, computed with quasioptical techniques [1], varies from −8.3 mm to −24 mm (negative sign → converging beam) and thus is always larger in magnitude than the corneal RoC. As a result, the reflected beam RoC is always smaller than the corneal RoC and thus diverges faster than the incident beam. If one considers the raypaths of the diverging beam, the rays near the beam center are more likely to be rerouted back to the detector system, which has a pin-hole like aperture. The marginal rays are either (1) steered away from the detector aperture at the aperture plane, or (2) walk-off the optical train altogether prior to arriving at the detector plane. This explanation is analogous to the operation of a confocal microscope in which the effective resolution of the imaging system is determined by both the focus of the source beam as well as the focus of the detector and the observed resolution exceeds that of the focused beam transverse extent.

VII. Corneal Phantom Imaging

A. Contact lens

The water content imaging capabilities of this system were explored by acquiring time-lapse images of a corneal phantom (soft contact lens) [10] undergoing desiccation. A contact lens was immersed in water for 5 minutes prior to imaging and then placed on a polypropylene ball identical in size to the calibration brass ball target (RoC = 8 mm). Then it was left to dry while THz images were consecutively acquired over a 30-minute period (Figure 12). The THz images were normalized to the brass sphere data and visualized the drying process of the contact lens from the thinner and exposed outer rim toward the center. This result is consistent with the behavior predicted by evaporation and diffusion, and correlates to the dynamics observed in the drying of flattened *ex vivo* cornea by [11].

A bright spot persisted in the upper right corner of the field of view throughout the drying process. This may be a thin film etalon effect from the coherence of the source and narrow, time averaged linewidth. We suspect this etalon was created by the warping and rolling of the edges of lens as it is dried, creating a small airgap in between the contact lens layers and the polypropylene ball. The net effect is a larger effective wave impedance and is consistent with the theory introduced in our earlier work [13, 14]. The behavior is repeatable but does not occupy the same location in the field of view further supporting the role of uncontrollable air gaps and the resulting in standing waves and subsequent constructive interference.

This experiment demonstrates THz reflectivity changes by hydration change are successfully captured by the imaging system. Overall signal return of sufficient SNR from the entire extent of the contact lens surface suggests the imaging system can effectively perform imaging of a human corneal target.

B. Ex vivo porcine eye

A final evaluation of the imaging design with phantoms was performed with *ex vivo* porcine (pig) eyes. Imaging this target enabled exploration of irregular surface profile and increased RoC effects on the imaging system design as pig eyes are slightly larger than human eyes and somewhat irregularly shaped. A visible image of the mounted pig eye is shown in the left panel of Figure 13(a) and its orientation in the imaging system is shown in Figure 13 (b).

The eye was immersed in 0.9% saline solution for 5 minutes before imaging in order to hyperhydrate the *ex vivo* tissue, and then imaged every ~ 2 minutes for 20+ minutes. This process was repeated for four separate *ex vivo* eyes. THz reflectivity maps were normalized using the brass ball (>95% reflectivity) data in Figure 9 to correct the field intensity non-uniformity due to coupling efficiency [1]. A representative time-series of one eye is displayed in Figure 13(c.1,2 – e.1,2) and demonstrates a loss in tissue hydration due to desiccation. The data displayed in Figure 13(c.1,d.1,e.1) was mapped to a sphere using equations (1) – (4). The *en face* representation of Figure 13(c.1,d.1,e.1) is shown in Figure 13(c.2,d.2,e.2). The average observed THz reflectivity of these specimen was 12±0.8 %.

The expected reflectivity of ex vivo corneal tissue could be computed by measuring the CTWC and using the methods discussed in [13,14]. At the end of imaging experiments, each cornea was resected, weighed, desiccated, and re-weighed. CTWC was computed as the ratio of dry weight to wet weight and the group had the water content between 84% and 86%. An expected THz corneal reflectivity of 11.7% was computed with 85% CTWC assuming no tear film and the CTWC gradient in the thickness dimension [13, 14]. The measured reflectivity consistently falls within the range of predicted reflectivity at 84%-86% CTWC.

VIII. In vivo Imaging

The imaging system was mounted on a modified ophthalmic examination table for imaging healthy human cornea (Figure 14). The volunteer placed their chin and head in the frame and their upper cheek against the alignment apparatus indicated by the upper red arrow in Figure 14 (a). Involuntary head and eye movement coupled with the narrow alignment tolerance of the fast OAP mirror rendered acquisition of consistent signal difficult. Therefore the 25.4 mm PFL OAP mirror (the imaging mirror) was replaced with a 38.1 mm PFL OAP mirror. The increased focal length produced a deeper depth of focus and provides more relaxed alignment requirement. The approximate scanned area of the 38.1 mm PLF OAP is denoted with the dotted circular contours in Figure 14 (b).

Imaging was performed three times in a row (3 minutes between each scan) on the same volunteer eye. Data was acquired row-by-row and the volunteer was instructed to blink between each row to maintain tear film integrity and reduce discomfort-induced movement arising from dryness. Each row scan was completed in < 1 second and the total acquisition time was less than 20 seconds. The the mapped THz reflectivity are displayed in Figure 14(c.1,d.1,e.1) and the *en face* representations are in Figure 14(c.2,d.2,e.2). These images were also normalized to the brass ball data.

At 650 GHz illumination, THz corneal reflectivity is dominated by the tear film and the first ~ 100 microns of the anterior stroma [14]. Measured *in vivo* tear film thickness ranges from ~4.79 ± 0.88 μm to more than 50 μm depending on the measurement technology [15]. It is likely that this measurement was not sensitive to corneal thickness (even assuming a tear film thickness of 4.79 μm) given the large absorption coefficient of stromal water and the relative increase in human corneal thickness compared to rabbit cornea [13, 14].

The observed average corneal reflectivity was 12% with a standard deviation of 2%. These numbers fall within the range of expected healthy cornea (79% water) reflectivity with a ~ 20 μm tear film. The repeatability of the measurement suggests that tear film thickness can be assessed with high frequency illumination and an assumed CTWC.

We believe this is the first, non-contact, *in vivo* THz images of a cornea ever published. While the results support the presented imaging system and theory, numerous practical challenges related to patient orientation and movement and need to be addressed. Further, precise characterization of CTWC from reflectivity measurements, in the presence of tear film, may will likely require additional measurement axes, e.g. coherent detection or

spectrally resolved data. These improvements will enable more quantitative analysis of *in vivo* cornea images.

IX. Discussion

Diffractions at the edges of the FOV, particularly the areas corresponding to the shortest scan radii, were observed in all the images of the characterization targets. These effects manifested as either increase or decreases in signal in areas where the known target reflectivities were not varying. While it is possible that that misalignment contributes nontrivially to this spurious signal, we believe that limiting the usable aperture to A-ω_0 may not be sufficient. Physical optics work is ongoing to explore these issues.

This work defined the geometry such that the mirror focal axis pierced the $(\theta, \phi) = (\pi/2, 0)$ in spherical coordinates and thus positioned the corneal apex to $(\pi/2, 0)$. Standard ophthalmologic imaging defines the geometry such that the major axis of an optical system and the corneal apex sit at $(\theta, \phi) = (0, 0)$ [16]. Equiangular scanning about the $(0, 0)$ point results in a substantial decrease in sampling density as the beam is traversed from the corneal apex to the periphery. This sampling density variation is significantly higher than that achieved with the $(\pi/2, 0)$ orientation which is why it was selected for this work.

The increased OAP mirror focal length resulted in a reduction in scanned solid angle. However, the reflector asymmetry was also reduced which we believe led to a mitigation of beam aberrations for small R_s.

X. Conclusions

This work presented the development of a novel THz corneal imaging system. Our first implementation employed a FMCW 650 GHz source and zero-bias Schottky diode detector. Images are reconstructed from three unique sampling schemes (Equiangular, Orthodromic, and Uniform Rectilinear). Images of characterization targets, constructed to assess spot size and field of view uniformity (coupling efficiency) were acquired. Fits between the extracted beam parameters and those predicted by quasioptical and physical optics analysis were presented. The image of uniformly reflective (brass ball) target demonstrated good agreement with the predicted optical coupling efficiency. The fits for the strip line target and step-response target displayed good correlation as a function of beam radius but the measured data consistently yielded focused spot radii that were less than what was predicted with both quasioptical and physical optics theories. This discrepancy was attributed to beam walk off due to surface profile discontinuities occurring at the interface between metallic and dielectric regions.

A corneal phantom (contact lens) was imaged and its spatially resolved reflectivity captured over a period of drying (30+ min.). *ex vivo* porcine eyes were also examined and further demonstrated the imaging system's hydration sensitivity.

Using a longer focal length imaging OAP mirror improved the target alignment tolerance of the system. With this modification, a non-contact THz image of a human cornea was acquired. The acquired THz reflectivity image and its signal profile are consistent with those

predicted by the quasioptical theory in [1]. Our experiments also identified some practical challenges that need to be addressed prior to starting larger human trials. Currently, we are implementing multi-rate sampling to increase image acquisition speed and reduce sensitivity to patient movement.

We believe that these results strongly support the feasibility of non-contact imaging of cornea *in vivo.* Our future studies aim to differentiate the critical differences in CTWC between the volunteers group with healthy cornea and patients group with corneal diseases.

Acknowledgments

References

1. Sung S, Dabironezare S, Llombart N, Selvin S, Bajwa N, Chantra S, Nowroozi B, Garritano J, Goell J, Li A, Deng SX, Brown E, Grundfest WS, Taylor ZD. Optical system design for non-contact, normal incidence, THz imaging of in vivo human cornea. Submitted to IEEE TTST. 2017

2. Gullstrand, A. Appendix. In: Helmholtz, HV., editor. Handbuch der physiologischen Optik. Vol. 1. New York: Dover; p. 351-352.351-352

3. Hjortdal JØ, Erdmann L, Bek T. Fourier analysis of video-keratographic data. A tool for separation of spherical, regular astigmatic and irregular astigmatic corneal power components. Ophthalmic and Physiological Optics. 1995; 15:171–185. [PubMed: 7659417]

4. RAASCH TW. Corneal Topography and Irregular Astigmatism. Optometry & Vision Science. 1995; 72:809–815. [PubMed: 8587769]

5. Mathworld, W. Great Circle. Mar 20. Available: http://mathworld.wolfram.com/GreatCircle.html

6. Goldsmith, P. Gaussian Beam Quasioptical Propogation and Applications. Piscataway, NJ: IEEE Press; 1998.

7. Madhow, U. Introduction to Communication Systems. Cambridge University Press; 2014.

8. Dunne MCM, Royston JM, Barnes DA. Normal variations of the posterior corneal surface. Acta Ophthalmologica. 1992; 70:255–261. [PubMed: 1609576]

9. Carney LG, Mainstone JC, Henderson BA. Corneal topography and myopia. A cross-sectional study. Investigative Ophthalmology & Visual Science. 1997; 38:311–320. [PubMed: 9040463]

10. Glass DH, Roberts CJ, Litsky AS, Weber PA. A Viscoelastic Biomechanical Model of the Cornea Describing the Effect of Viscosity and Elasticity on Hysteresis. Investigative Ophthalmology & Visual Science. 2008; 49:3919–3926. [PubMed: 18539936]

11. Bennett DB, Taylor ZD, Tewari P, Singh RS, Culjat MO, Grundfest WS, Sassoon DJ, Johnson RD, Hubschman J-P, Brown ER. Terahertz sensing in corneal tissues. Journal of Biomedical Optics. 2011; 16:057003–057003. [PubMed: 21639581]

12. Bennett DB, Taylor ZD, Sassoon D, Tewari P, Johnson RD, Singh R, Culjat MO, Hubschman J-P, Grundfest WS. Terahertz sensing in corneal tissues. J Biomed Opt. 16:8.

13. Taylor ZD, Garritano J, Shijun S, Bajwa N, Bennett DB, Nowroozi B, Tewari P, Sayre JW, Hubschman JP, Deng SX, Brown ER, Grundfest WS. THz and mm-Wave Sensing of Corneal Tissue Water Content: In Vivo Sensing and Imaging Results. Terahertz Science and Technology, IEEE Transactions on. 2015; 5:184–196.

14. Taylor ZD, Garritano J, Sung S, Bajwa N, Bennett DB, Nowroozi B, Tewari P, Sayre J, Hubschman JP, Deng S, Brown ER, Grundfest WS. THz and mm-Wave Sensing of Corneal Tissue Water Content: Electromagnetic Modeling and Analysis. Terahertz Science and Technology, IEEE Transactions on. 2015; 5:170–183.

15. Werkmeister RM, Alex A, Kaya S, Unterhuber A, Hofer B, Riedl J, Bronhagl M, Vietauer M, Schmidl D, Schmoll T, Garhöfer G, Drexler W, Leitgeb RA, Groeschl M, Schmetterer L.

Measurement of Tear Film Thickness Using Ultrahigh-Resolution Optical Coherence TomographyUltrahigh-Resolution OCT Measurement of Tear Film. Investigative Ophthalmology & Visual Science. 2013; 54:5578–5583. [PubMed: 23847319]

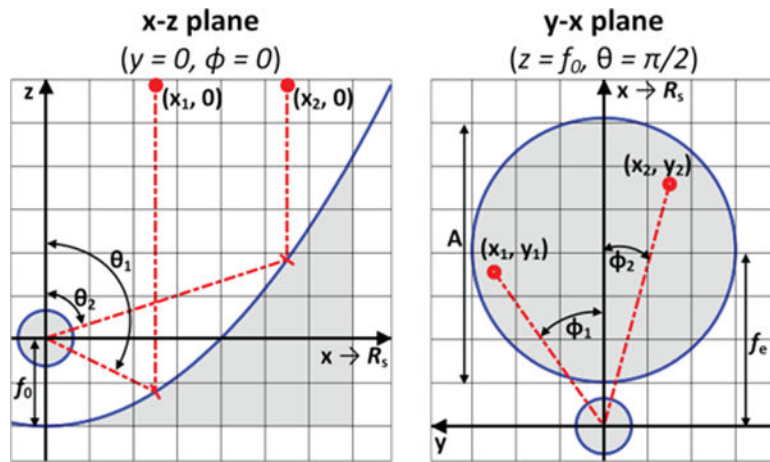16. Rao SK, Padmanabhan P. Understanding corneal topography. Current Opinion in Ophthalmology. 2000; 11:248–259. [PubMed: 10977769]

Figure 1.
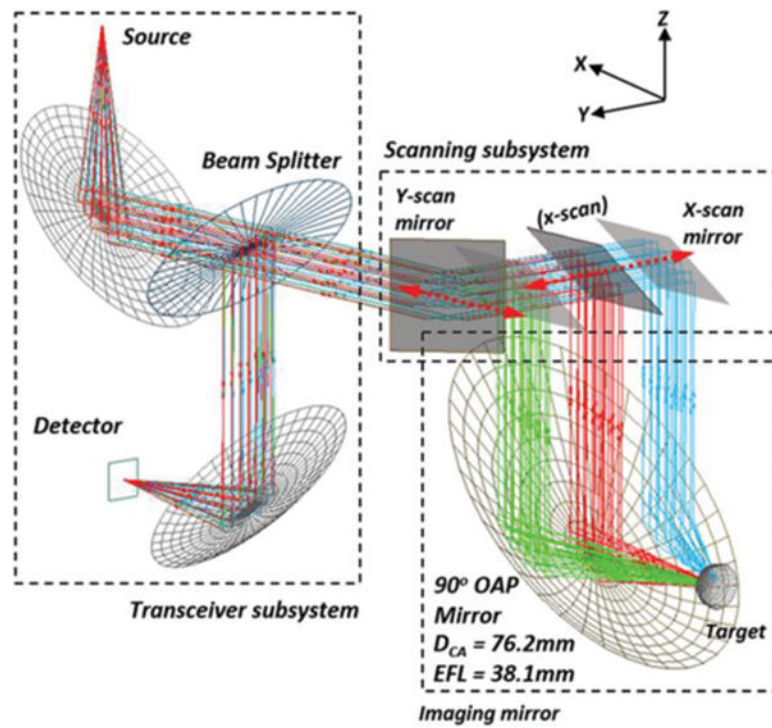Mapping of the transverse coordinates of the mirror CA (x, y) to the angular coordinates of the cornea (θ, ϕ).

Figure 2.
Single mirror scanning imaging system design comprised of three distinct subsystems. The raypath originates at the source, passes through the scanning mirrors, reflects off the cornea, and then retrace its path back to the detector.
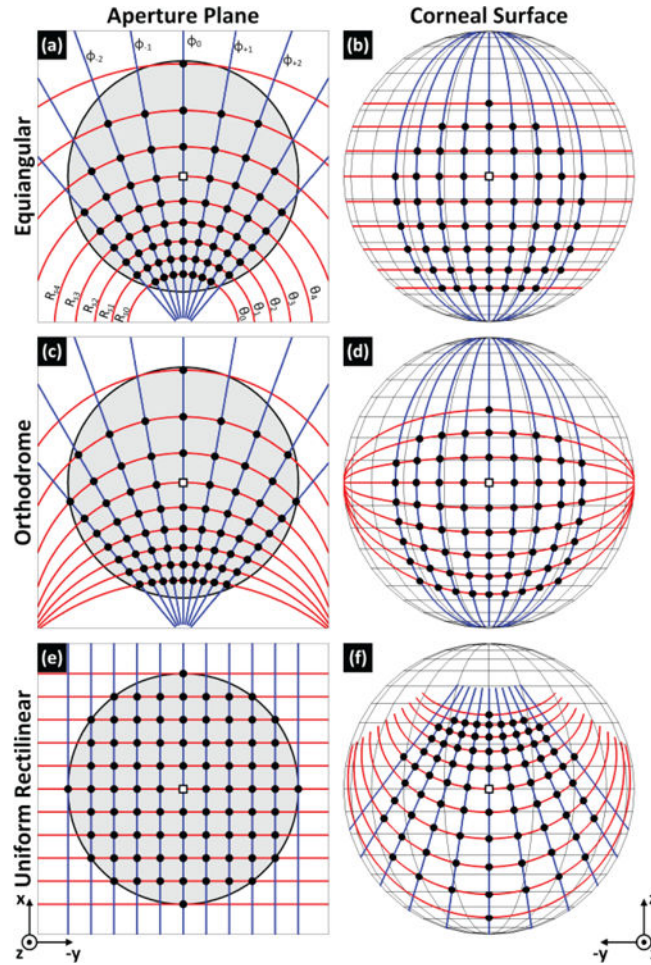
Figure 3.
Mappings between the clear-aperture (CA) plane of a 90°, 76.2mm CA, 25.4 PFL OAP mirror and an 8 mm radius sphere (cornea). Equiangular sampling in the (a) mirror clear aperture space and (b) corneal (spherical) space. (c), (d): Orthodromic sampling. (e), (f): Uniform Rectilinear sampling. The orthodromic and spherical scan lines are shown with 5° separation on the corneal surface. The uniform rectilinear scanning is shown with a 5 mm sample separation in the CA plane. The black circle markers (●) correspond to scan line intersections are that falls within the mirror CA. The "longitude" and "latitude lines" are denoted with the blue and red traces respectively.
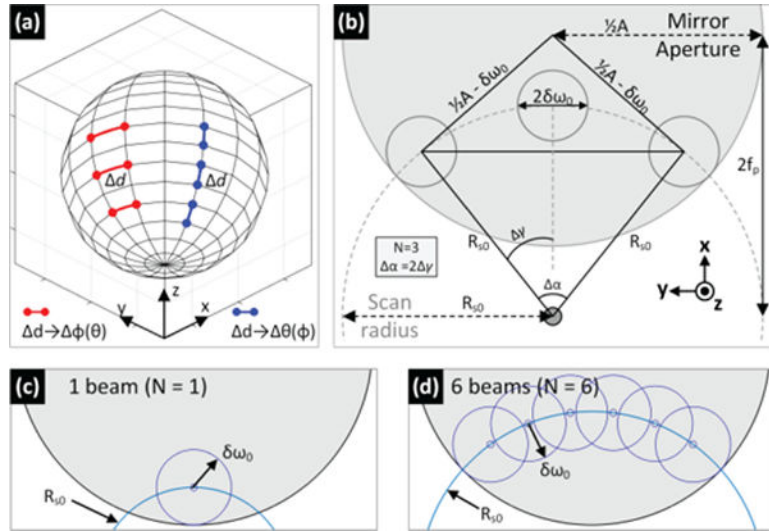
Figure 4.
Computing optimal beam packing: (a) spherical chords for varying (θ, ϕ). (b) Geometry set-up for computing the initial scan radius. Beam packing with one beam (c) and 6 beams (d) on the first radial scan line. Due to the varying focal length of the OAP, the near edge of the mirror must be densely sampled.
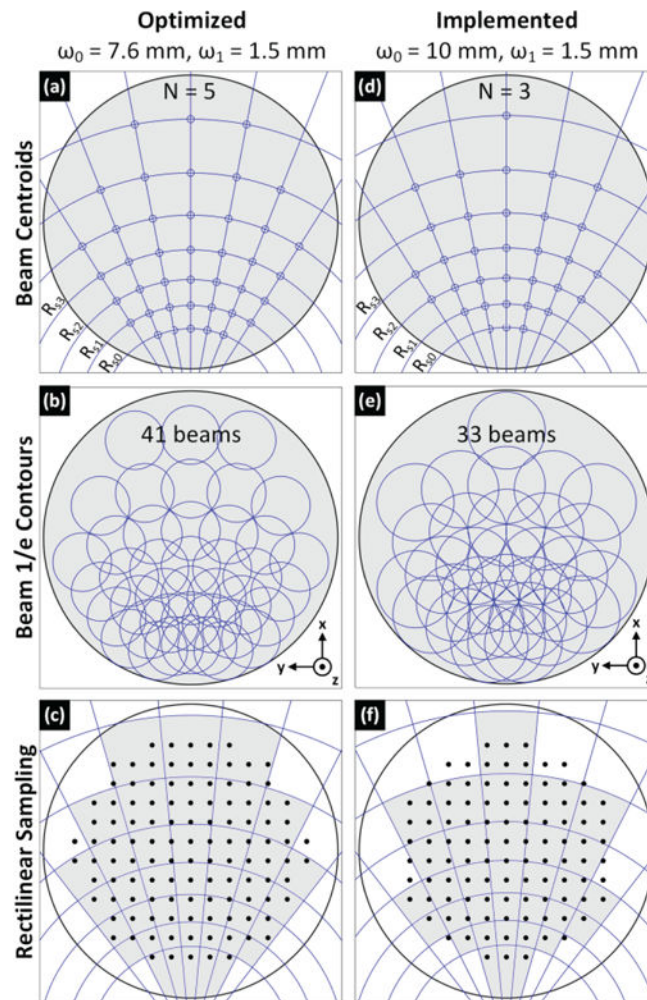
Figure 5.
(a) Equiangular sampling scheme for a 7.6 mm input beam radius and 1.5 mm center-to-center sample spacing. (b) 1/e beam diameters centered at each mapped sample location, (c) mapped sample location regions with superimposed rectilinear sampling grid. (d) – (f) same as (a) – (c) for an input beam radius of 10 mm and output sampling of 1.5 mm.
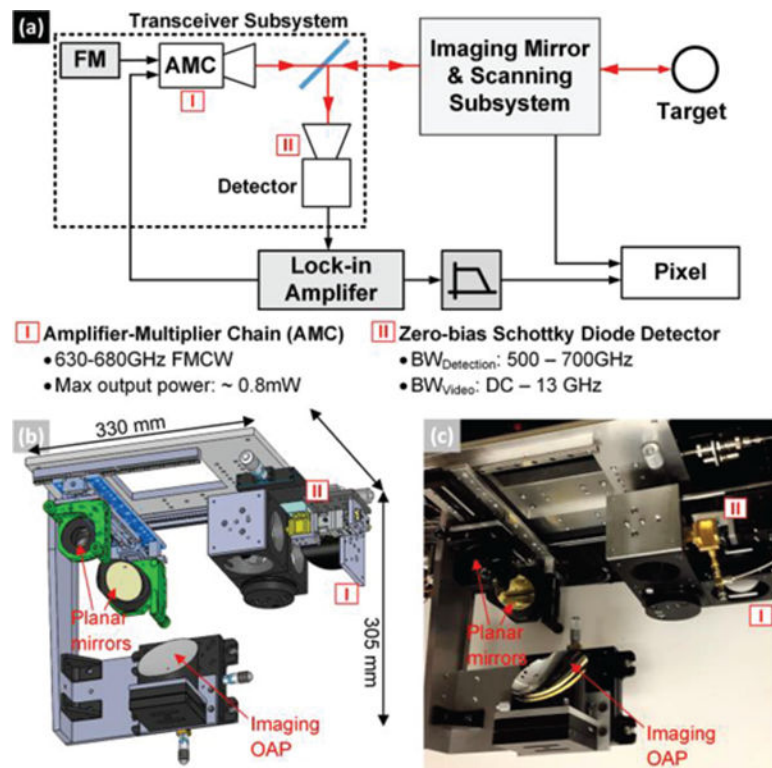
Figure 6.
(a) Block diagram of the imaging system employing an FMCW THz source and zero-bias Schottky diode detector. (b) CAD rendering and (c) photograph of the imaging system.
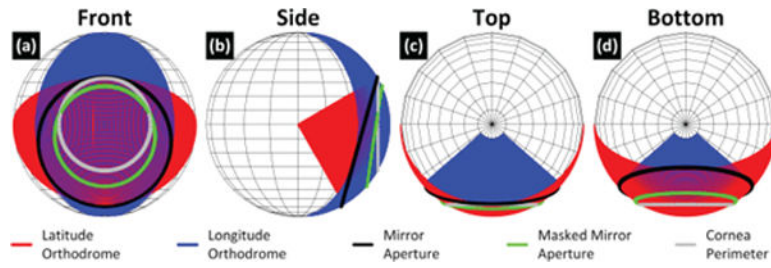
Figure 7.
Corneal field of view (FOV) subtended by a 76.2 mm CA, 25.4 PFL OAP. The black circle on the surface denotes the mapped CA of the OAP. The gray circle denotes the extent of the cornea. Orthodromic scan lines that span the extent of the mapped mirror aperture are shown in red and blue.
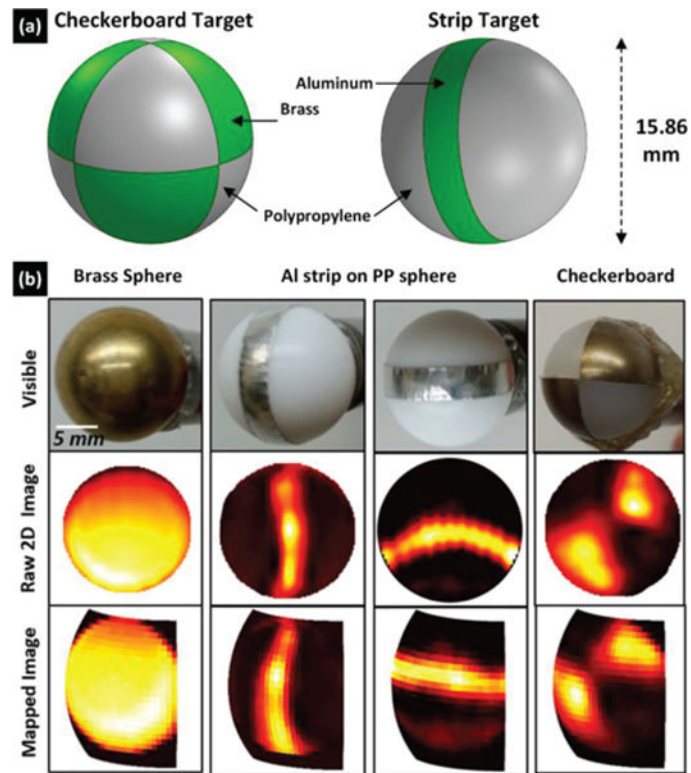
Figure 8.
(a) CAD drawings of characterization targets. (b) Images at 650 GHz. *Top row*: photographs of characterization targets; *Middle row*: raw images (clear aperture images) of characterization targets.; *Bottom row*: mapped images of characterization targets. THz images are displayed in the standard "hot" color map.
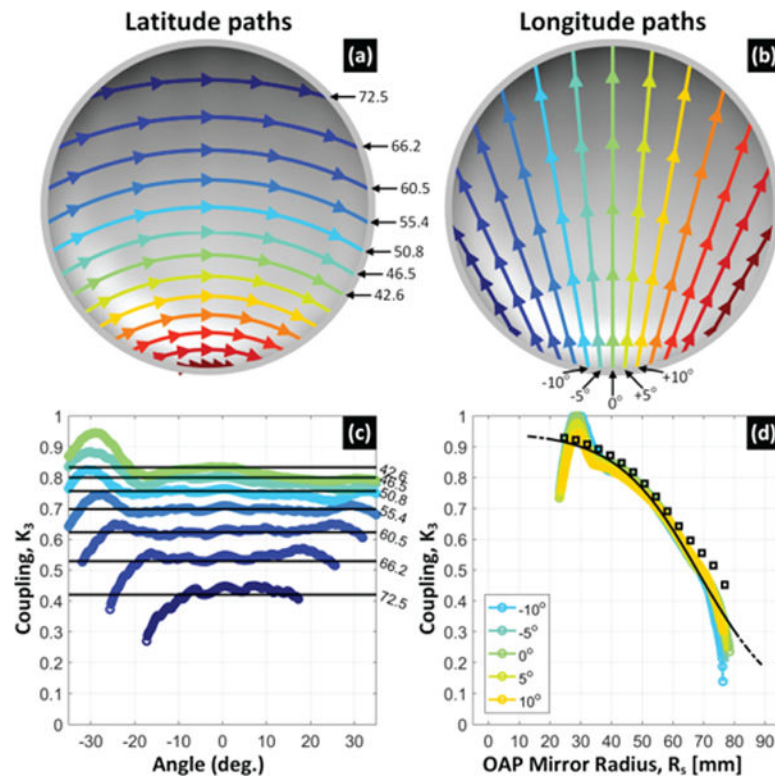
Figure 9.
Coupling calibration target. (a) Latitude (equiangular) scan lines superimposed on the imaging data, (b) Longitude (equiangular) scan lines on the imaging data, (c) latitude scan profiles, and (d) longitude scan profiles with fit to equation (6).
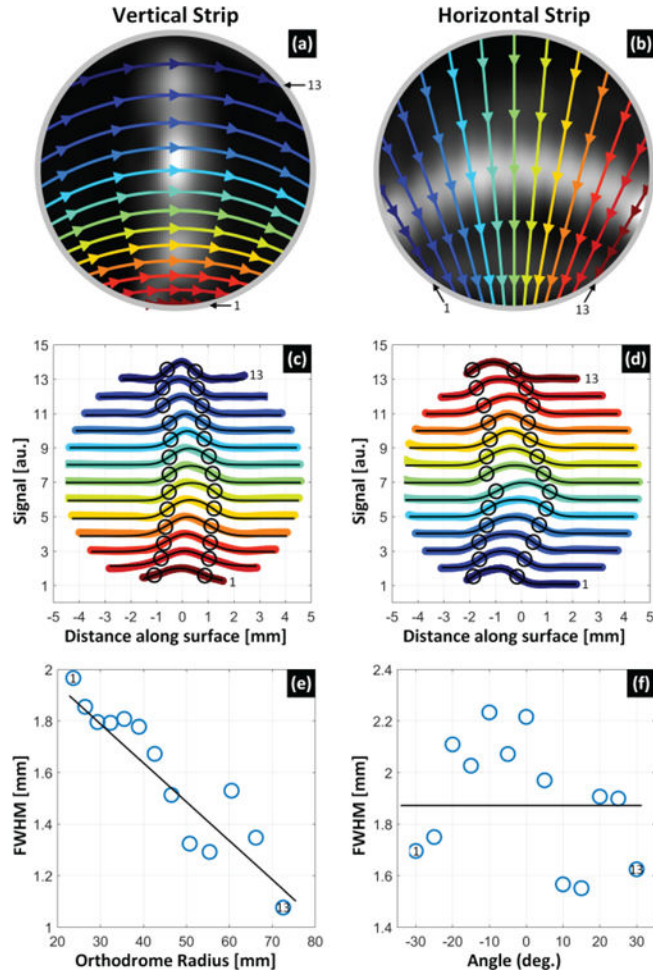
Figure 10.
Metallic strip resolution target. (a) Orthodrome scan lines orthogonal to the vertical strip orientation, (b) Orthodrome scan lines orthogonal to the horizontal strip orientation, (c) Image profiles from the vertical strip orientation, (d) Image profiles from the horizontal strip orientation. (e) extracted FWHM from the vertical strip orientation, (f) extracted FWHM from the horizontal strip orientation. "Orthodrome Radius" in (e) refers to the distance from the mirror focal point to the center of the orthodromic scan lines (ϕ =0).
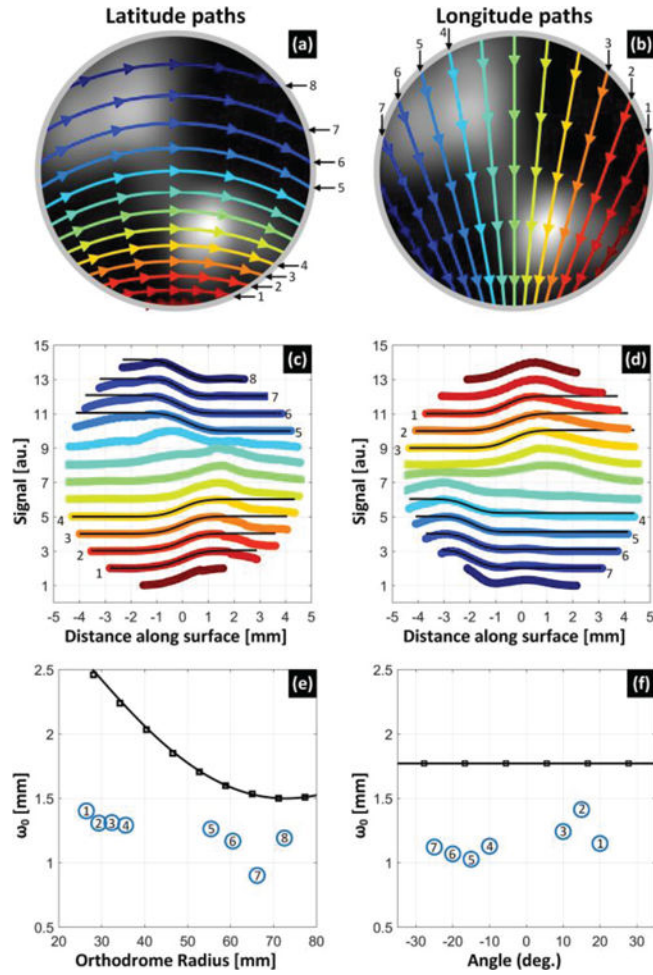
Figure 11.
Checkerboard target. (a) Orthodromic scan lines orthogonal to the vertical edges, (b) Orthodromic scan lines orthogonal to the horizontal edges, (c) Image profiles from the vertical edges, (d) Image profiles from the horizontal edges, (e) extracted 1/e field radius from the vertical edges, (f) extracted 1/e field radius from the horizontal edges. "Orthodrome Radius" in (e) refers to the distance from the mirror focal point to the center of the orthdromic scan lines ($\phi = 0$).
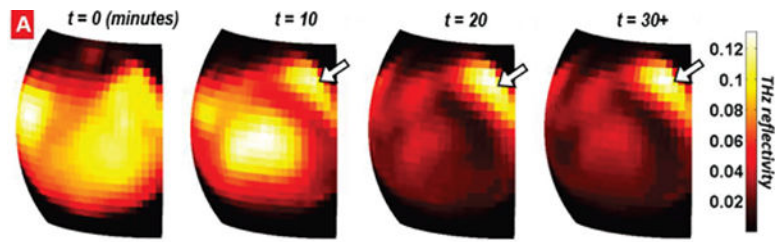
Figure 12.
Time lapse images of drying contact lens (left to right). Reflectivity correlates to the hydration state of the lens. Drying from the outer rim mirrors results obtained with planar scanning [12]. The persistent reflectivity in the top right corner of the FOV, indicated by the arrow, map be an etalon artifact arising from a thin air gap created by geometric distortion as the sample dried.
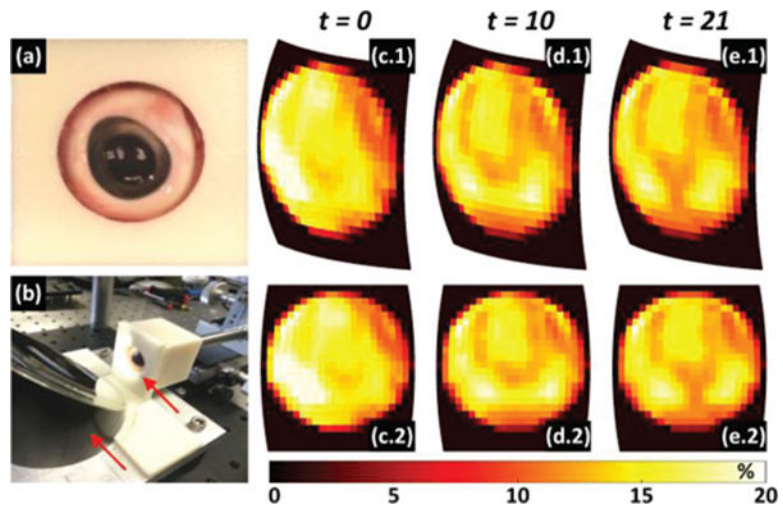
Figure 13.
Time lapse images of drying *ex vivo* porcine. (a) Eye placed in a polypropylene mount. (b) Mounted eye positioned in the THz imaging system. (c.1, d.1, e.1) Brass ball normalized, data mapped at t = 0 mins, 10 mins, and 21 mins. (c.2, d.2, e.2) *En face* view of (c.1, d.1, e.1).
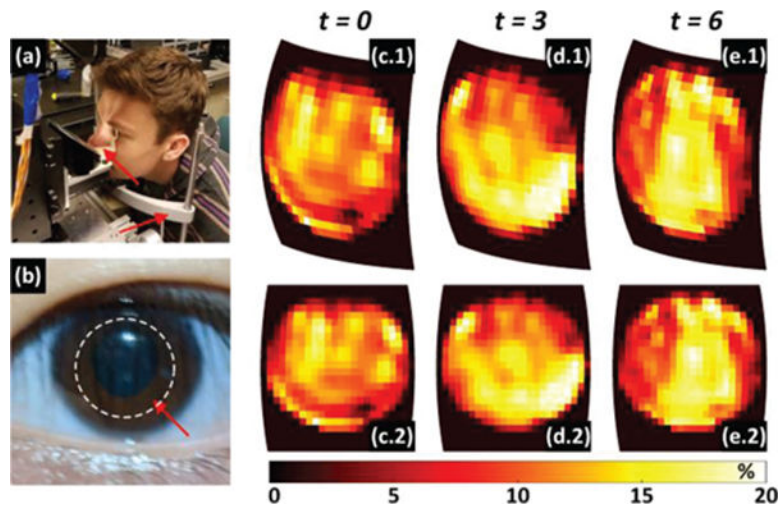
Figure 14.
Non-contact, *in vivo*, human cornea imaging. (a) volunteer positioned in front of the imaging system. (b) Visible image of volunteer's eye with approximate FOV denoted by the dotted contour. (c.1, d.1, e.1) Brass ball normalized, data mapped at t = 0 mins, 3 mins, and 6 mins. (c.2, d.2, e.2) *En face* view of (c.1, d.1, e.1).